

AD-A262 863



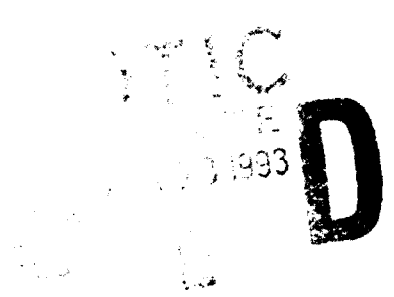
WL-TR-92-3107

An Upwind Method for the Solution of the 3D Euler and Navier-Stokes Equations on Adaptively Refined Meshes

Michael. J. Aftosmis
Computational Aerodynamics Group
Aerodynamics and Airframe Branch
Aeromechanics Division

October 1992

Final Report for Period March 1991 - June 1992



Approved for public release; distribution unlimited



FLIGHT DYNAMICS DIRECTORATE
WRIGHT LABORATORY
AIR FORCE MATERIEL COMMAND
WRIGHT-PATTERSON AIR FORCE BASE, OHIO 45433-6553

93-07357



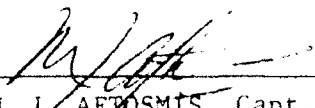
4921

NOTICE


When Government drawings, specifications, or other data are used for any purpose other than in connection with a finitely Government-related procurement, the United States Government incurs no responsibility or any obligation whatsoever. The fact that the government may have formulated or in any way supplied the said drawings, specifications, or other data, is not to be regarded by implication, or otherwise in any manner construed, as licensing the holder, or any other person or corporation; or as conveying any rights or permission to manufacture, use, or sell any patented invention that may in any way be related thereto.

This report is releasable to the National Technical Information Service (NTIS). At NTIS, it will be available to the general public, including foreign nations.

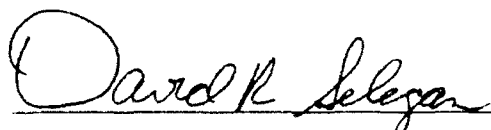
This technical report has been reviewed and is approved for publication.



MICHAEL J. AFROSMIS, Capt, USAF
Aerospace Engineer



W. PHILLIP WEBSTER, Tech Mgr
CFD Research Section



DAVID R. SELEGAN
Chief
Aeromechanics Division

If your address has changed, if you wish to be removed from our mailing list, or if the addressee is no longer employed by your organization please notify WL/FIMM. WPAFB, OH 45433- 6553 to help us maintain a current mailing list.

Copies of this report should not be returned unless return is required by security considerations, contractual obligations, or notice on a specific document.

REPORT DOCUMENTATION PAGE			Form Approved OMB No 0704 0188	
Public reporting burden for this collection of information is estimated to average 1 hour per response, including the time for reviewing instructions, searching existing data sources, gathering and maintaining the data needed, and completing and reviewing the collection of information. Send comments regarding this burden estimate or any other aspect of this collection of information, including suggestions for reducing this burden, to Washington Headquarters Service, Project for Information Operations and Reports, 1215 Jefferson Davis Highway, Suite 1204, Arlington, VA 22202-4302, and to the Office of Management and Budget, Paperwork Reduction Project (0704-0188), Washington, DC 20503.				
1. AGENCY USE ONLY (Leave blank)	2. REPORT DATE 17 Oct 92	3. REPORT TYPE AND DATES COVERED Final Report Mar 91 - Jun 92		
4. TITLE AND SUBTITLE An Upwind Method for the Solution of the 3D Euler and Navier-Stokes Equations on Adaptively Refined Meshes			5. FUNDING NUMBERS PE: 61102F PR: 2307 TA: N6 WU: 11	
6. AUTHOR(S) Michael J. Aftosmis (513-255-7127)				
7. PERFORMING ORGANIZATION NAME(S) AND ADDRESS(ES) Flight Dynamics Directorate Wright Laboratory (WL/FIMM) Air Force Materiel Command Wright-Patterson AFB OH 45433-6553			8. PERFORMING ORGANIZATION REPORT NUMBER WL-TR-92-3107	
9. SPONSORING/MONITORING AGENCY NAME(S) AND ADDRESS(ES) Flight Dynamics Directorate Wright Laboratory (WL/FIMM) Air Force Materiel Command Wright-Patterson AFB OH 45433-6553			10. SPONSORING/MONITORING AGENCY REPORT NUMBER	
11. SUPPLEMENTARY NOTES Completely in-house research, conducted with the DLR in Braunschweig, Germany. Submitted for publication in AIAA Journal.				
12a. DISTRIBUTION/AVAILABILITY STATEMENT Approved for public release; distribution unlimited			12b. DISTRIBUTION CODE	
13. ABSTRACT (Maximum 200 words) A new node based upwind scheme for the solution of the 3D Navier-Stokes equations on adaptively refined meshes is presented. The method uses a second-order upwind TVD scheme to integrate the convective terms, and discretizes the viscous terms with a new compact central difference technique. Grid adaptation is achieved through directional division of hexahedral cells in response to evolving features as the solution converges. The method is advanced in time with a multistage Runge-Kutta time stepping scheme. Two- and three- dimensional examples establish the accuracy of the inviscid and viscous discretization. These investigations highlight the ability of the method to produce crisp shocks, while accurately and economically resolving viscous layers. The representation of these and other structures is shown to be comparable to that obtained by structured methods. Further 3D examples demonstrate the ability of the adaptive algorithm to effectively locate and resolve multiple scale features in complex 3D flows with many interacting, viscous, and inviscid structures.				
14. SUBJECT TERMS Computational Fluid Dynamics Unstructured Meshes, Upwind Methods			15. NUMBER OF PAGES 49	
			16. PRICE CODE	
17. SECURITY CLASSIFICATION OF REPORT Unclassified	18. SECURITY CLASSIFICATION OF THIS PAGE Unclassified	19. SECURITY CLASSIFICATION OF ABSTRACT Unclassified	20. LIMITATION OF ABSTRACT UL	

Table of Contents

List of Figures	iv
Acknowledgements	vi
1. Introduction	1
2. Description of Method	3
2.a Governing Equations	3
2.b Spatial Integration of Convective Fluxes	4
Implementation of Convective Discretization	8
2.c Spatial Integration of Viscous Fluxes	10
Implementation of Viscous Discretization	12
2.d Eigenvalue Scaling for High Aspect Ratio Cells	14
3. Adaptation	15
3.a Feature Detection	15
Shock Detection	16
Smooth Feature Detection	16
Directional Division	17
3.b Interfaces	19
4. Numerical Investigations and Results	22
4.a Fundamental Issues	22
4.b 3D Viscous Flow	28
4.c Processing Efficiency and Storage	36
5. Summary and Future Work	38
6. References	39
Nomenclature	42

List of Figures

Figure 1.	Formation of dual mesh of <i>Auxiliary Cells</i> in two and three dimensions.....	5
Figure 2.	Cell nomenclature required for construction of the numerical flux, \bar{Q}_k , through face k of cell i	7
Figure 3.	Difference stencil for second-order upwind representation of the flux function $\bar{\Phi}_W$ at the west face of cell i	9
Figure 4.	Construction of <i>Secondary Cell</i> for the calculation of first derivatives on the E face of the auxiliary cell which surrounds node i . (Left: 2D, Right: 3D).....	13
Figure 5.	Schematic of adaptation map for directional division of hexahedral cells in two and three dimensions.....	18
Figure 6.	Physical and auxiliary cells at interfaces between levels of divided cells in two and three dimensions.....	20
Figure 7.	Final adapted mesh (1500 nodes) and Mach No. distributions along rays A and B for inviscid 2D flow over circular cylinder.	23
Figure 8.	Inviscid double wedge corner flow test case. $M_\infty = 2.98$, $\delta_1 = \delta_2 = 9.49^\circ$, 70,000 nodes.	25
Figure 9.	Mach contours in plane at $x = 0.8$ superimposed upon shock positions from inviscid gasdynamic theory [24] experimental data [25] and previous inviscid calculation [26].	26
Figure 10.	Convergence history of RMS sum of all state vector residuals.	27
Figure 11.	Flat plate boundary layer calculation. $M_\infty = 0.5$, $Re_L = 5,000$. Comparison of u -velocity profile with Blasius solution at various levels of mesh resolution.....	29

Figure 12. Flat plate boundary layer calculation. $M_\infty = 0.5$, $Re_L = 5,000$. Comparison of skin friction with Blasius solution at various levels of mesh resolution..... 30

Figure 13. Navier-Stokes solution of supersonic flow over delta wing of Ref [27] at $M_\infty = 1.2$, $Re_C = 480,000$, $\alpha = 20^\circ$ with 999,000 nodes..... 32

Figure 14. Total pressure loss contours at t.e. ($x = 1.0$) showing shock induced separation..... 33

Figure 15. Mesh and Mach contours in symmetry plane..... 34

Figure 16. Right: Results from experimental oil flow visualization [27] ($Re_C = 2.4-5.3 \times 10^6$). Left: Computed surface streamlines from numerical solution ($Re_C = 4.8 \times 10^5$). Left: Comparison of C_p at $x = 0.8$ with experimental results from Ref. [27]..... 35

Accession For	
NTIS	<input checked="" type="checkbox"/>
DTIC	<input type="checkbox"/>
AD	<input type="checkbox"/>
JAERI	<input type="checkbox"/>
By _____	
Date _____	
Approved by _____	
Dist	Availability Statement
A-1	

Acknowledgments

This work was accomplished within a scientific exchange program between the USAF and the Deutsche Forschungsanstalt für Luft und Raumfahrt e.V. during the author's stay as a visiting scientist at DLR Braunschweig. Financial support for this exchange was provided by the SEEP program and is gratefully acknowledged. Computing support was provided by both the DLR and the Phillips Laboratory Supercomputing Center at Kirtland AFB. The author would like to sincerely thank Dr. N. Kroll for his invaluable contributions to this work and the exchange as a whole. Additionally, the many contributions of U. Hermann and Dr. R. Radespiel are gratefully acknowledged.

1. Introduction

The accurate simulation of flows with features spanning many length scales presents a major challenge to Computational Fluid Dynamics. This issue becomes especially critical in 3D flows over complex configurations, or even flows over simple configurations at extreme flow conditions, where multiple interacting 3D features must be correctly represented.

The last decade has seen the emergence of two basic approaches to surmounting this fundamental difficulty. High resolution upwind schemes attempt to represent shocks and contact discontinuities with as few cells as possible [1-6], while adaptive grid techniques automatically adjust the local mesh dimension in an attempt to resolve the scale of the local flow physics [5-9]. Therefore, the combination of a high resolution upwind algorithm with unstructured mesh adaptation suggests a natural and extremely flexible platform for simulating flow fields with features spanning a variety of disparate length scales. The current work adopts this combined approach and uses adaptively refined hexahedral meshes to provide a foundation for a second order upwind algorithm based upon the "Upwind TVD" technique of Harten and Yee [10].

Mesh adaptation through directional cell division forms a flexible and efficient procedure for resolving finer length scales within the flow field [8,6]. The technique avoids the limited nature of grid redistribution algorithms, and minimizes computational expense since points are only added in regions of the simulation which require further enhancement. This flexibility requires a solver capable of dividing an arbitrary collection of cells and

necessitates fully unstructured data storage. Despite the use of hexahedral meshes, and often, structured *looking* starting meshes, the solver must be free of assumptions about mesh topology, and must treat any mesh as simply a collection of cells with some explicitly defined connectivity.

Although interest is currently growing in truly multidimensional [11] and multidirectional [12] upwind techniques, most successful and robust upwind techniques still rely upon successive application of essentially one dimensional operators through space operator splitting. On triangular or tetrahedral meshes, the implementation of higher order upwind operators (with their large discretization stencils) is not straightforward, and several approaches have been suggested in the recent literature [13,14]. The use of hexahedral cells, however, provides a clear mapping of this discretization stencil onto the domain, while avoiding the ambiguities associated with higher order upwind stencils on triangular meshes [6]. Additionally, such meshes easily provide the high quality regular mesh near wall boundaries that is necessary for accurate evaluation of the viscous fluxes in the Navier-Stokes equations.

Nearly all unstructured techniques require an initial mesh to begin the numerical simulation. In the current method, this mesh typically begins as a single or multiple block structured mesh. Thus, a good quality background mesh must still be generated by conventional techniques and the flexibility afforded by the Delauny, advancing front, or other techniques available for generating tetrahedral meshes is not currently available for hexahedral meshes. This drawback is, however, no more severe than it is for structured techniques, and is largely offset by both the natural mapping of the upwind operator and accuracy advantage offered by the use of hexahedral cells in viscous regions.

2. Description of Method

The numerical method relies upon Harten and Yee's "Upwind TVD" algorithm [10] to integrate the inviscid fluxes while the viscous terms use central difference modeling. This spatial discretization is advanced in time through a modified Runge-Kutta procedure. An option for central differencing of the inviscid fluxes also exists. This option is essentially a node-based version of the well known central scheme by Jameson with blended second and fourth order artificial dissipation [15]. The central difference option was included primarily to permit direct comparison of discrete solutions from upwind and central difference simulations on identical adapted meshes.

2.a Governing Equations

The Navier-Stokes equations describe the unsteady flow of a viscous gas and may be written in integral form for a general 3D region V .

$$\iiint_V \frac{\partial \bar{U}}{\partial t} dV = - \oint_{\partial V} \bar{F} \cdot \bar{n} ds \quad (1)$$

$$\bar{F} = \bar{F}_I - \bar{F}_V \quad (2)$$

Here, \bar{U} is the state vector of conserved variables, and \bar{F} is the complete tensor of flux density which contains both viscous and inviscid components. ∂V is the closed boundary of V with the outward facing unit normal vector $\bar{n} = [n_x, n_y, n_z]^T$. This set of equations is closed through the assumption of a calorically perfect gas, and adopting the Stokes Hypothesis.

Assuming an isotropic, Newtonian fluid yields a symmetric shear stress tensor. Constant Prandtl number modeling is assumed throughout the domain, and Sutherland's Law describes the variation of viscosity with temperature.

2.b Spatial Integration of Convective Fluxes

The spatial discretization of the governing equations may be conveniently developed by focusing on the symbolic form of the equations given by expression {1}. Considering a control volume fixed in time, and applying the mean value theorem, this equation may be recast as

$$\left(\frac{\partial \bar{U}}{\partial t}\right)_V = -\oint_{\partial V} \bar{F}_I \cdot \bar{n} ds + \oint_{\partial V} \bar{F}_V \cdot \bar{n} ds \quad \{3\}$$

The inviscid and viscous integration implied by eq.{3} proceeds on a dual mesh formed by connecting the geometric centers of the physical mesh cells which surround each node. Figure 1 shows construction of this dual *auxiliary* mesh in two and three dimensions. The state vector of conserved quantities is stored at nodal locations. Expression {3} may be further specialized for application to a specific polyhedral control volume, V_i , with planar faces, and may then be approximated by:

$$\begin{aligned} \frac{\partial \bar{U}_{V_i}}{\partial t} &= -\frac{1}{V_i} \sum_{k \in \partial V_i} \bar{F}_{I_k} \cdot \bar{S}_k + \frac{1}{V_i} \sum_{k \in \partial V_i} \bar{F}_{V_k} \cdot \bar{S}_k \\ \frac{\partial \bar{U}_{V_i}}{\partial t} &= -\frac{1}{V_i} \sum_{k \in \partial V_i} \bar{Q}_k + \frac{1}{V_i} \sum_{k \in \partial V_i} \bar{F}_{V_k} \cdot \bar{S}_k \end{aligned} \quad \{4\}$$

where k denotes the k^{th} face of volume V_i and $\bar{S}_k = [S_x, S_y, S_z]^T$ is the surface vector of face k . The first term on the R.H.S. of eq.{4} approximates the inviscid surface integral, while the second term balances the viscous fluxes through the faces of the cell around i .

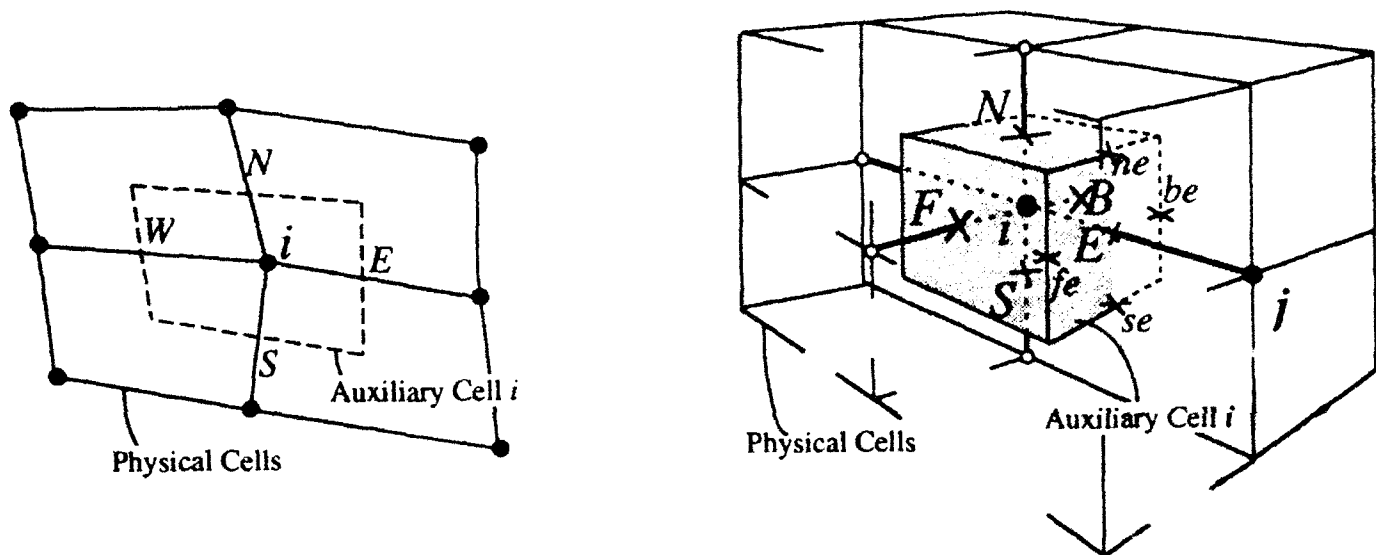


Figure 1. Formation of dual mesh of *Auxiliary Cells* in two and three dimensions.

Evaluating the summation for the inviscid flux balance requires computation of the numerical flux, \bar{Q}_k , through each face k . Using the notation found in Figure 2, an upwind formulation of this flux may be expressed as

$$\bar{Q}_k = \frac{1}{2}(\bar{F}_L + \bar{F}_R) \cdot \bar{S}_k + \frac{1}{2} \mathfrak{R}_k \bar{\Phi}_k \quad (5)$$

Here $()_L$ and $()_R$ denote conditions to the left and right of face k and \mathfrak{R} is the right eigenvector matrix of the flux Jacobians in transformed space. Eq.(5) separates \bar{Q}_k into a summation of a symmetric term constructed like a central difference operator and a term which adapts this stencil in accordance with local wave propagation.

Two formulations of the flux function, $\bar{\Phi}_k$, were suggested by Yee which lead to second-order TVD schemes [1]. The present method is the less dissipative of the two, and relies upon the "modified flux" approach of Harten. With $l = 1, \dots, 5$, the l^{th} component of $\bar{\Phi}_k$ may be written as

$$\Phi_k^l = \frac{1}{2} \Psi(\lambda_k^l)(g_L^l + g_R^l) - \Psi(\lambda_k^l + \gamma_k^l) \alpha_k^l \quad (6)$$

$$\text{with } \bar{\alpha}_k = \mathfrak{R}_k^{-1}(\bar{U}_R - \bar{U}_L) \quad (7)$$

leads to Harten and Yee's "Upwind TVD" scheme [10]. In eq.(7) $\bar{\alpha}_k$ would be the difference of the characteristic variables from $()_R$ to $()_L$ if \mathfrak{R}_k^{-1} were evaluated at the right and left states individually. Instead, the nonlinear nature of the governing equations forces us to evaluate the inverse of the right eigenvector matrix at face k at an intermediate state and we employ the approximate Riemann solver developed by Roe to define this state. Here, λ^l are the eigenvalues of the transformed flux Jacobians. If the wave speed, λ^l , were to vanish, the asymmetric term on the R.H.S. of eq.(6) would also vanish and thus violate the entropy condition [2]. To prevent this, $|\lambda^l|$ in eq.(6) is thresholded near zero by introducing the functions $\Psi(z)$ and γ_k^l .

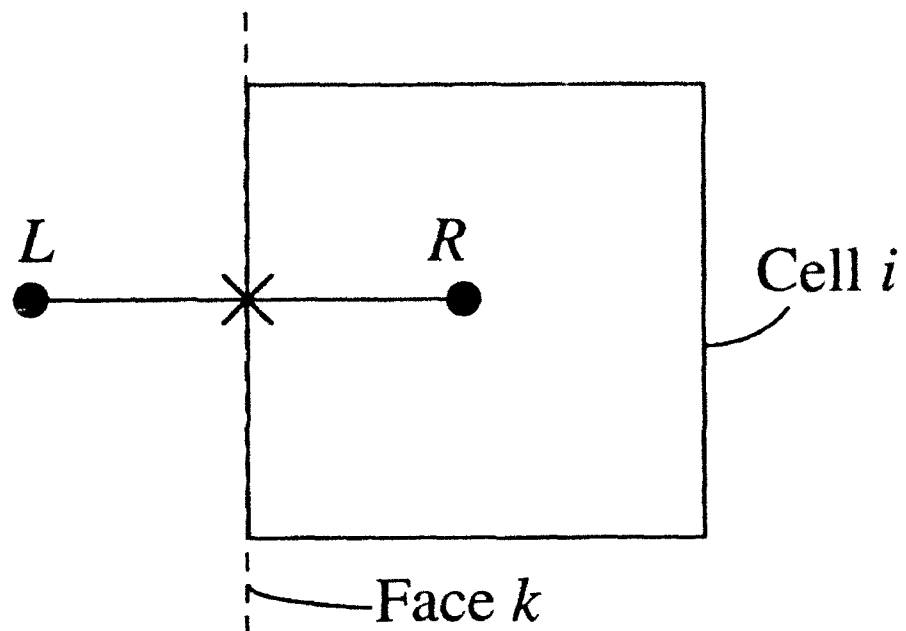


Figure 2. Cell nomenclature required for construction of the numerical flux, \bar{Q}_k , through face k of cell i .

$$\Psi(z) \equiv \begin{cases} |z| & |z| \geq \delta \\ \frac{(z^2 + z^2)}{2\delta} & |z| < \delta \end{cases}, \text{ with } \delta \ll 1 \quad (8)$$

$$\text{and } \Psi(z) \equiv \begin{cases} |z| & |z| \geq \delta \\ \frac{(z^2 + \delta^2)}{2\delta} & |z| < \delta \end{cases}, \text{ with } \delta \ll 1 \quad (9)$$

The limiter function, g^l , appearing in eqs. {6} and {9} is taken from Ref. [16]. Notice that setting this limiter identically to zero degenerates the entire method to Roe's first order scheme. The implementation of [17] provides a basis for the current node-based formulation (see also [6]).

Implementation of Convective Discretization

Adopting this node-based implementation results in a convenient approach for the construction of an unstructured adaptive algorithm, while still permitting accurate and straightforward treatment of boundaries. In developing this algorithm, the inviscid flux balance of eq.{3} is evaluated using midpoint quadrature, and thus the numerical flux, \bar{Q}_k , must be evaluated at the center of each auxiliary cell face.

Figure 3 shows the stencil required by eqs.{3} and {6} to form the complete numerical flux through the west face of V_i . These expressions emphasize that the first order ($\bar{g} \equiv 0$) upwind approximation of the inviscid flux requires only nearest neighbor information. However, as shown in the exploded view of this stencil, the complete flux function on the west face of this cell, $\bar{\Phi}_W$ -required for a second-order approximation - depends on information from beyond the nearest neighbor. This observation reemphasizes the fundamental difficulty in the design of higher order upwind methods on unstructured meshes.

This dilemma is alleviated through reexamination of the formulation presented by eqs. {6-9}. These expressions divide the formation of the complete stencil into a sequence of operations

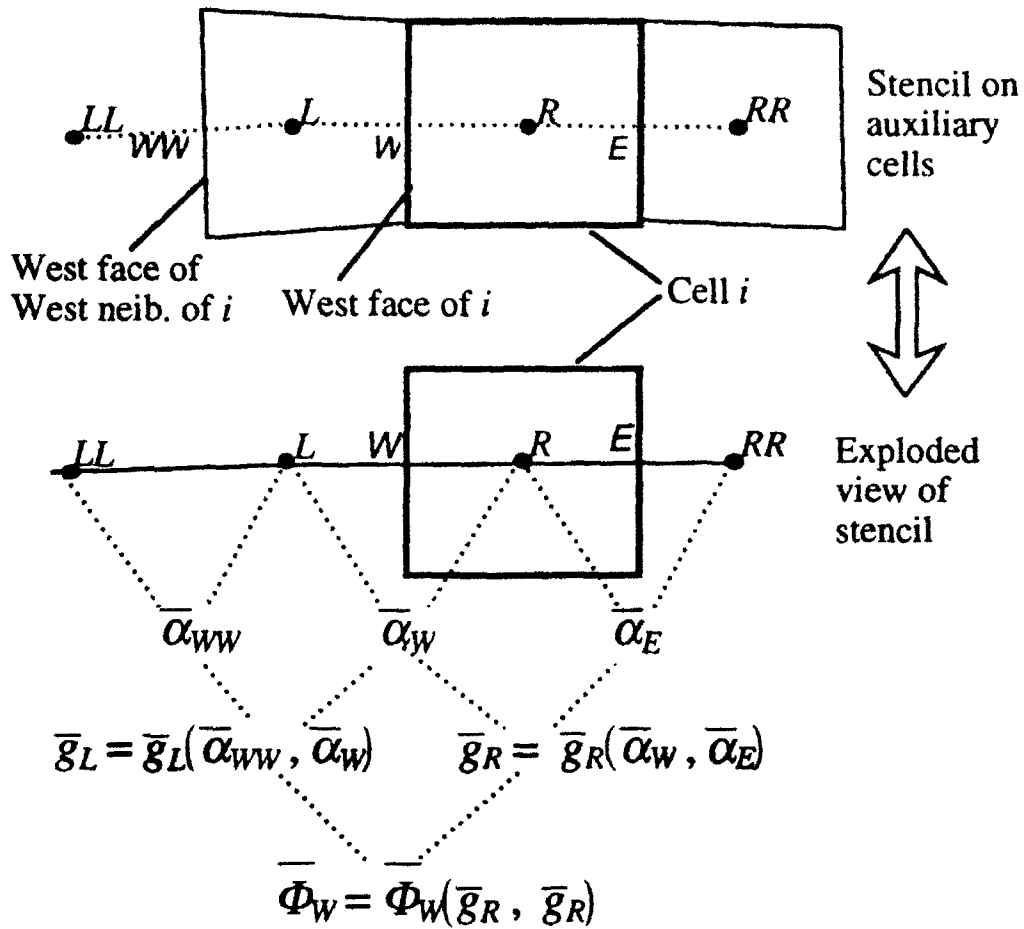


Figure 3. Difference stencil for second-order upwind representation of the flux function $\bar{\Phi}_W$ at the west face of cell i .

within which no single step requires communication beyond the nearest neighbor. By first calculating $\bar{\alpha}_k$ across all the faces of all cells on the auxiliary mesh, and then storing these values in each cell, the limiters \bar{g}_k - and therefore the flux function $\bar{\Phi}_k$ - may be evaluated by simply interrogating only the auxiliary cell immediately to the west of cell V_i and V_i itself. Breaking up the second-order discrete operator into these two successive steps forms the complete update to the state vector at i with only nearest neighbor inquiries.

This multiple pass evaluation of the upwind difference stencil is analogous to the splitting of the fourth order dissipation operator in an unstructured central difference scheme. In such schemes, the fourth difference stencil is too large to be computed with only nearest neighbor information, so it is usually evaluated by taking the second difference of a set of second differences which were precomputed in a previous sweep [9]. Similarly, the current procedure forms the limiter \bar{g} as a function of the difference of characteristic variables that were precalculated in a prior step. The additional memory requirements implied by this strategy are not severe as will be shown in a subsequent section.

2.c Spatial Integration of Viscous Fluxes

The inviscid integration scheme may be extended to the full Navier-Stokes equations by a separate discretization of the viscous components of the flux density tensor. As suggested by the form of eq.{4}, the complete update to any node, $\Delta \bar{U}_i$, is a summation of inviscid and viscous contributions.

$$\Delta \bar{U}_i = (\Delta \bar{U}_i)_I + (\Delta \bar{U}_i)_V \quad \{10\}$$

The viscous discretization uses central difference modeling and the selection of control volumes is similar to that found in Ref. [8]. The choice of central differencing allows the scheme to be written extremely compactly, and eventually it involves only node-to-cell and cell-to-node communication while organizing all gather-scatter operations so that they may be easily grouped for rapid processing. These communication issues remain important

because the current implementation uses a cell based data structure (like that in [8] and [7]) and each physical cell can address only the nodes at its vertices directly. Thus an implementation based upon cell-to-node operations is especially convenient.

Its worth noting that this basic discretization is also amenable to edge-based data structures. In fact, Ref. [18] describes the formulation of Hessian and Laplacian operators using only edge-based formulas. For the hexahedral based meshes discussed here, however, this strategy holds little obvious advantage, and so the cell-based formulas were used.

Ref. [19] contains a complete development of the viscous discretization in two and three dimensions. The intent of this section is to provide an outline of that discretization so that the important implementational issues may be clearly understood. The complete viscous discretization may be illustrated by considering the formation of the model second derivative term u_{xx} at node i . Recalling the previous assumption that the control volume V_i has planar faces and applying the Gauss divergence theorem on the surface ∂V_i of auxiliary cell V_i in Fig.1 gives

$$\begin{aligned} (u_{xx})_i &= \frac{1}{V_i} \oint_{\partial V_i} (u_x) n_x dS \\ &= \frac{1}{V_i} [(u_x)_E S_x^E - (u_x)_W S_x^W + (u_x)_N S_x^N - (u_x)_S S_x^S + (u_x)_F S_x^F - (u_x)_B S_x^B] \end{aligned} \quad \{11\}$$

The x -components of both the unit normal vector, n_x , and the surface vector, S_x , are taken oriented in positive coordinate directions. With the auxiliary cells constructed as described above, each edge incident upon node i will always pierce the face of an auxiliary cell. Thus, eq.(11) contains one contribution from each edge terminating at i . This observation becomes increasingly important when integrating more general polyhedral control volumes.

Eq.(11) makes use of first derivatives, u_x , at the N, S, E, W, F, B faces. A second surface integral, similar to this expression, provides each of these quantities at the required midface

location. This is accomplished by constructing a secondary set of control volumes which surround each of the edges incident upon node i . Figure 4 illustrates the *secondary cell* constructed around the edge piercing the E face of auxiliary cell i in 2 and 3D.

$$\begin{aligned} (u_x)_E &= \frac{1}{V_E} \oint_{\partial V_E} u n_x dS \\ &= \frac{1}{V_E} [u_j S_x^j - u_i S_x^i + u_{ne} S_x^{ne} - u_{se} S_x^{se} + u_{fe} S_x^{fe} - u_{be} S_x^{be}] \end{aligned} \quad (12)$$

V_E is the volume of the secondary cell. Eq. (12) requires the surface vectors for the East secondary cell, and these are constructed by averaging the surface vectors from the faces of the auxiliary cells surrounding nodes i and j (the nodes which define the end points of the edge which pierces the E face of V_i).

$$\begin{aligned} (\bar{S}^{ne})_{V_E} &= \frac{1}{2}(\bar{S}_i^N + \bar{S}_j^N) , & (\bar{S}^{se})_{V_E} &= \frac{1}{2}(\bar{S}_i^S + \bar{S}_j^S) , & (\bar{S}^{fe})_{V_E} &= \frac{1}{2}(\bar{S}_i^F + \bar{S}_j^F) \\ (\bar{S}^{be})_{V_E} &= \frac{1}{2}(\bar{S}_i^B + \bar{S}_j^B) , & (\bar{S}^j)_{V_E} &= \frac{1}{2}(\bar{S}_j^W + \bar{S}_j^E) , & (\bar{S}^{ne})_{V_E} &= \frac{1}{2}(\bar{S}_i^N + \bar{S}_j^N) \end{aligned} \quad (13)$$

Similar constructions around the remaining edges which meet at i form the remaining first derivatives needed to evaluate (11). The choice of this set of secondary control volumes, and the use of the Divergence Theorem ensures that the secondary control volumes are closed, and that the viscous discretization remains free stream preserving on any arbitrary mesh. Furthermore, this discretization is completely conservative and the formulation recognizes and damps odd-even decoupling on stretched or unstretched meshes [19].

Implementation of Viscous Discretization

Unstructured implementation of the discretization outlined by eqs. (11) and (12) essentially reduces to rearranging these expressions to match the data structure. Within the current cell-based structure, the operations comprising these two surface integrals are broken up into contributions from each physical mesh cell. Operations are then performed within each mesh

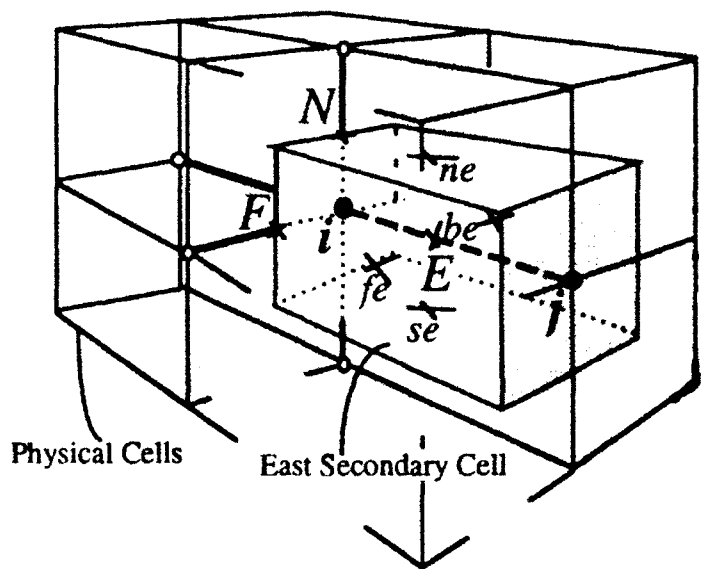
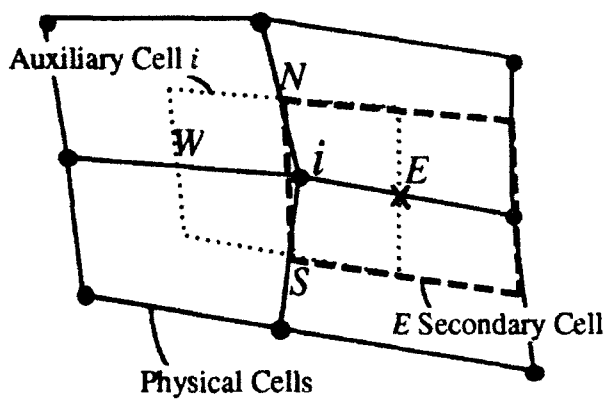


Figure 4. Construction of *Secondary Cell* for the calculation of first derivatives on the *E* face of the auxiliary cell which surrounds node i . (Left: 2D, Right: 3D).

cell, and contributions are distributed to each of the cell vertices (nodes). This process forms the complete update at the mesh nodes. In visualizing this, note that the first derivatives required by eq.(11) are located on the faces of the auxiliary cells. These locations correspond to mid-edges of the physical mesh. Thus, the algorithm sweeps through the physical mesh on a cell-by-cell basis, forming the viscous fluxes along the edge of the physical cells, and finally balancing these fluxes on the auxiliary cells to form the nodal update. The actual implementation is discussed fully in [19] and is based upon the 2D work of [20]. Implicit in this approach is the fact that under the assumptions of a Newtonian Fluid, the viscous flux calculation becomes a linear combination of first derivative quantities.

2.d Eigenvalue Scaling for High Aspect Ratio Cells

Near wall boundaries, high aspect ratio cells are commonly used to efficiently resolve the boundary layer. Since the artificial dissipation is scaled isotropically with the spectral radius of the flux Jacobian matrices, the damping in the wall normal direction may become excessive. Ref. [21] proposed a 3D extension to the 2D variable scaling proposed by Martinelli [22] which adjusts levels of the blended 2nd and 4th order smoothing used in conjunction with the central difference option for the convective flux discretization. When the TVD convective dissipation is chosen, this nonisotropic scaling affects only the waves which are subject to the entropy cutoff. In the current work, all waves are cut in Euler simulations, while in viscous simulations, only the nonlinear ($u \pm a$) waves are subject to this cutoff. In such cases, this scaling takes a form similar to that found in [23].

3. Adaptation

The adaptation algorithm increases the resolution of the discrete solution by locally reducing the mesh spacing. The algorithm begins by scanning a preliminary (coarse) solution for regions of interest. It then enhances the mesh in those regions through the addition of new computational nodes. These new points are currently added through cell division [7], and the position of all mesh nodes may then be modified by a redistribution step which provides more smoothly varying grid metrics without altering mesh connectivity.

3.a Feature Detection

The crisp shocks afforded by the TVD integration scheme may be detected by undivided differences of several parameters. However, in problems involving high speed flow where several parameters may jump by orders of magnitude through a shock (*e.g.*, static pressure), there exists a danger of overlooking less prominent features with a crude detection algorithm. Furthermore, recent studies of various feature detection strategies demonstrate that failure to adapt to smooth, less prominent features may lead to an adaptive procedure which actually converges to the wrong solution [23]. For these reasons, a new procedure has been developed which separates shock recognition from the detection of other flow features.

Several other factors contribute to this decision. The current algorithm captures shocks with only two or three cells [6,17] because the difference stencil can change structure to reflect the different nature of the governing equations on either side of such an interface. With a characteristic thickness of only a few mean free paths, a shock is one of the very few flow

structures which will always be much smaller than the local mesh dimension (in a continuum situation). Thus, while the adaptation will eventually embed several computational cells across most other flow features, this will not occur at shocks. Such reasoning gives both physical and numerical motivation for treating shock detection in a special manner.

Shock Detection

A normalized, undivided second difference of pressure provides a parameter which is quite sensitive to both strong and weak shocks. Such a quantity recognizes curvature in the pressure profile across a three point difference stencil. Thus, it is well suited to recognize the step-like profiles associated with the discrete shocks expected from the TVD scheme [1,17]. Additionally, it performed well in the study of refinement parameters provided in [7]. This second difference is then normalized by a weighted average of local pressures in order to reduce its magnitude at strong shocks, and increase its size at weak ones.

Reference [6] contains a complete formulation of this *shock refinement parameter*, R_s , and any physical cell with R_s exceeding some threshold (usually 0.05) is tagged for division as a "shock cell." Although somewhat empirical in basis, this procedure very reliably locates shocks in trans- super- and hypersonic flow. Moreover, the overall detection algorithm is quite insensitive to the precise threshold value chosen. The primary drawback of this parameter lies in the fact that it may mistakenly tag a strong expansion fan as a "shock." Nevertheless, most features which contain strong nonlinearity usually warrant detection, and this is not a serious shortfall.

Smooth Feature Detection

With the cells near strong nonlinearities successfully identified, only the remaining cells are then rescanned for smoother, less prominent features. With these extrema removed, the remaining field may be considered "smooth," and features may be located on a statistical basis as in Ref. [20]. Undivided differences of total velocity (scaled as in [23]) and density

provide a basis for locating inviscid features. A second sweep using an undivided second difference of velocity magnitude is used to locate regions of rapidly varying shear stress to identify poorly resolved viscous layers in Navier-Stokes simulations. All physical cells containing values of the refinement parameter above a threshold set 20 percent above the mean are tagged for division.

Directional Division

The current adaptive procedure identifies not only a feature's location, but also its orientation. Many flow features are predominantly one-dimensional and are frequently almost aligned with the coarse base grid. With this information, the hexahedral cells may be divided directionally to avoid excessive resolution in directions where resolution requirements are more relaxed. In three dimensions, this means that a cell may be divided in only one or two directions. Such refinements create only one or three additional cells, rather than the seven which are created if each cell always divides in all three directions.

As the detector scans the field, it stores refinement parameters for each physical cell in all three computational directions. Figure 5 contains a sketch of an adaptation map (in both 2 and 3D) within which all the cells in a two- or three-dimensional domain will lie. Using the notation on the figure, each cell will have some $[R_\xi, R_\eta, R_\zeta]$ coordinate and will plot on this map. The threshold, T , mentioned in the preceding section appears as a quarter sphere on this figure, and all cells outside it become marked for refinement. Furthermore, the location of the cells on this map indicate the directions in which the cells require refinement. The rays which delineate different regions emanate from the origin and are currently set at an angle of 15° .

To avoid the formation of excessive interface regions between cells at different levels of refinement, directional adaptation was used only at the finest level of cell division [20,6]. This final division typically creates from 50 percent (2D) to 75 percent (3D) of the final

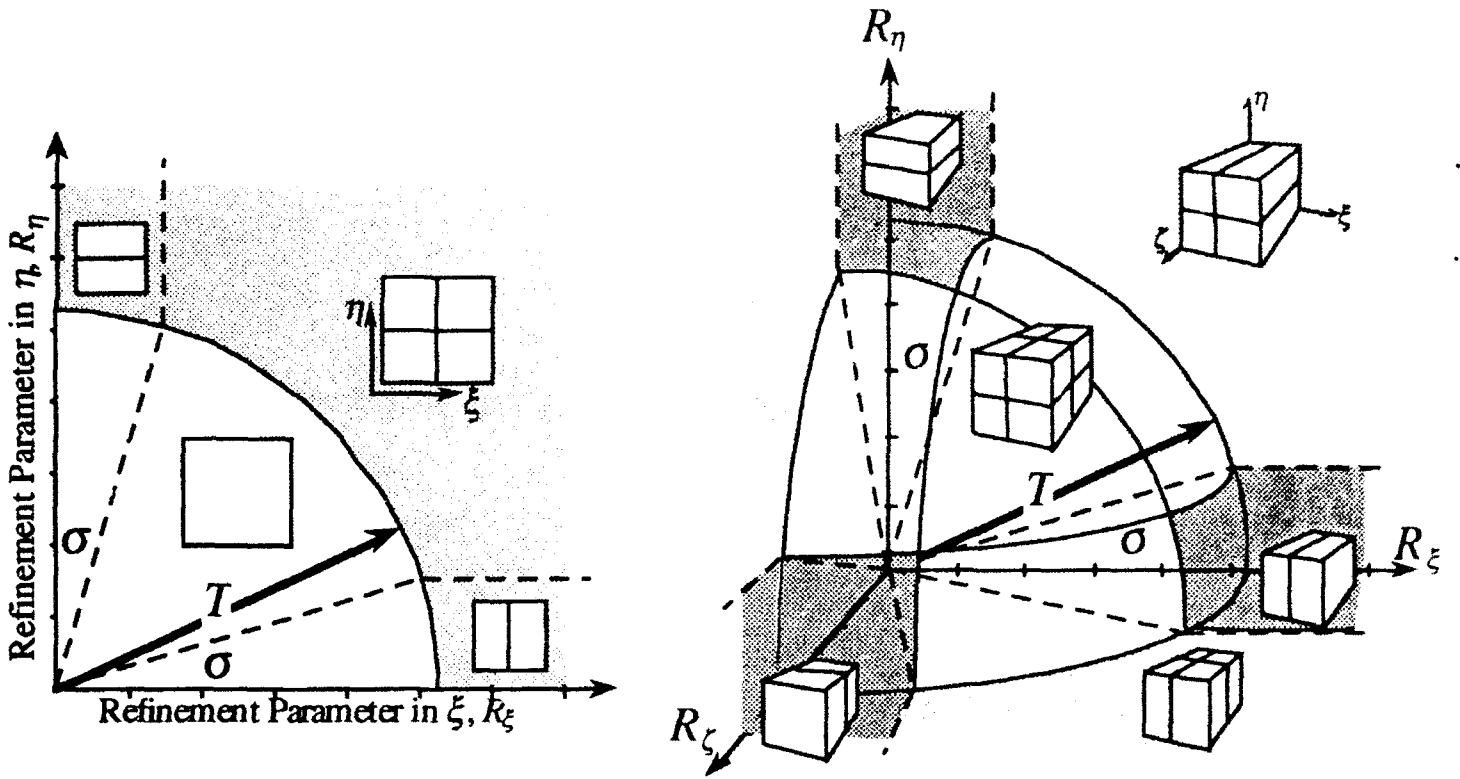


Figure 5. Schematic of adaptation map for directional division of hexahedral cells in two and three dimensions.

nodes in the mesh, and directional division typically reduces the total number of new nodes created by about 50 percent in both 2 and 3D.

4.b Interfaces

An essential complication of hexahedral cell division is the appearance of interfaces between different levels of physical cells. Figure 6 shows a region of divided cells bordering on an undivided region in 2 and 3D. For simplicity, the cells have been divided in all directions. Shown at the left of this figure are the physical cells, and on the right are the auxiliary cells formed by connecting the centers of the physical cells. In 2D, this construction results in the formation of triangular auxiliary cells around hanging nodes like *B*. In 3D midface nodes (like *B*) are surrounded by a pyramidal auxiliary cell and midedge nodes, like *C*, are surrounded by prismatic cells. All of these auxiliary cells may be adopted into the framework by permitting a degeneracy in the North surface vector ($\bar{S}_N \equiv 0$) of auxiliary cells *B* and *C* and integrating the resulting cells without special treatment.

Since the node-based formulation proceeds by interacting the auxiliary cells, without special care, all cells whose difference stencil crosses the interface will suffer a first order stretching error in the calculation of derivatives across this interface. Focusing on the 2D example in the upper half of the figure, this means that although cells like *A* and *P* have complete difference stencils, in regions where flow properties vary faster than linearly, these differences will be contaminated by mesh stretching. Triangular, prismatic, or pyramidal cells also suffer a stretching error, but, more importantly, their difference stencil is left incomplete. For example, cell *B* has no northern neighbor which gives rise to a degeneracy in the northern extension of the difference stencil of *B*. This deficiency is overcome by linearly interpolating for the missing α (eq. (7)) from the α_N on the north faces of *A* and *C* (in the 2D case). The treatment of *B* as a degenerate cell whose northern surface vector is zero retains storage space for the interpolated $(\alpha_N)_B$. Such a quantity is required by the limiter on the south face of cell *B* when second-order accuracy is sought.

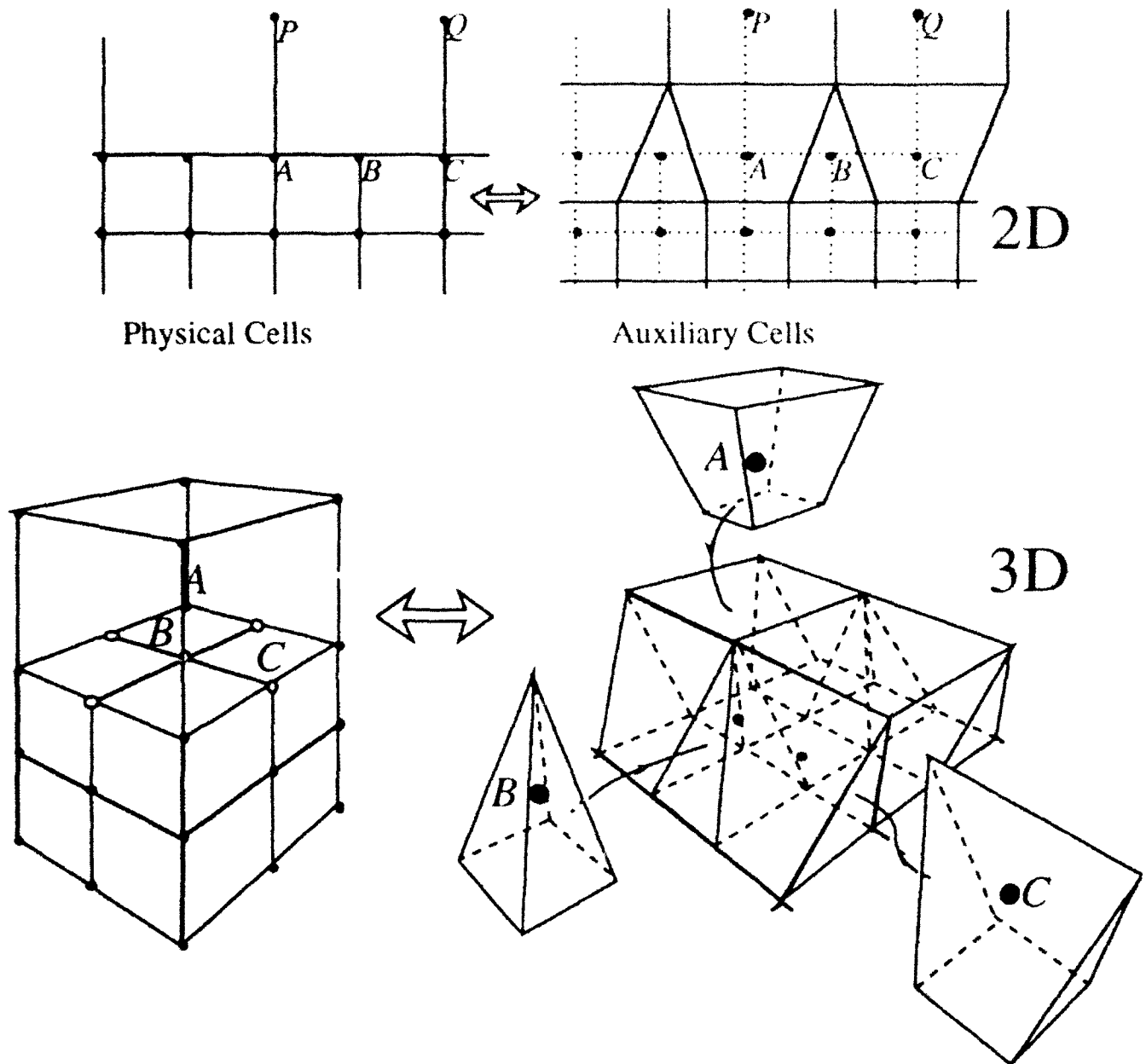


Figure 6. Physical and auxiliary cells at interfaces between levels of divided cells in two and three dimensions.

These ideas form a simple and effective strategy for treating the interfaces which appear in adaptive hexahedral meshes. First, the centers of all physical cells are used to define the auxiliary mesh. Then, if a degenerate cell is encountered while sweeping to calculate the difference of characteristic variables, $\bar{\alpha}_k$, the missing $\bar{\alpha}_k$ stem from a combination of the $\bar{\alpha}_k$ on similar faces of its neighboring cells. This treatment permits a complete operator to be formed on the face opposite the degeneracy, and after filling in the missing $\bar{\alpha}_k$, the flux balance for the prismatic or pyramidal cells proceeds without special handling. This simple treatment is both conservative and robust. It suffers only from the same stretching error experienced by any node whose stencil is similarly stretched. The viscous update to the interface nodes proceeds upon the same set of control volumes.

4. Numerical Investigations and Results

The presentation of numerical results is organized to first establish the validity of the solving procedure and then to examine global aspects of the adaptive methodology. The investigations focus on topologically simple example problems which are designed to first establish the accuracy of the inviscid and viscous discretization, and then to examine the ability of the adaptation to correctly locate and resolve structures in complex 3D flows with interacting viscous and inviscid features. Unless specifically noted, all numerical results presented use the Upwind TVD formulation for the numerical flux.

4.a Fundamental Issues

This section begins with a brief examination of shock and boundary layer resolution, preservation of monotonicity, and other basic issues of the numerical modeling. The first numerical example considers inviscid flow over a 2D circular cylinder exposed to a Mach 8.03 cross flow. The left half of Figure 7 contains the final adapted mesh (1,500 nodes), and line plots of local Mach number are included to the right. These Mach number distributions follow a ray tracing outward from the centerline, and along another line inclined 36° from vertical. As is evident from the grid, directional division was employed at the finest level of refinement.

All cases presented in this paper were computed using the limiter function, g^l , taken from Ref. [16] (Eq. 3.51f)

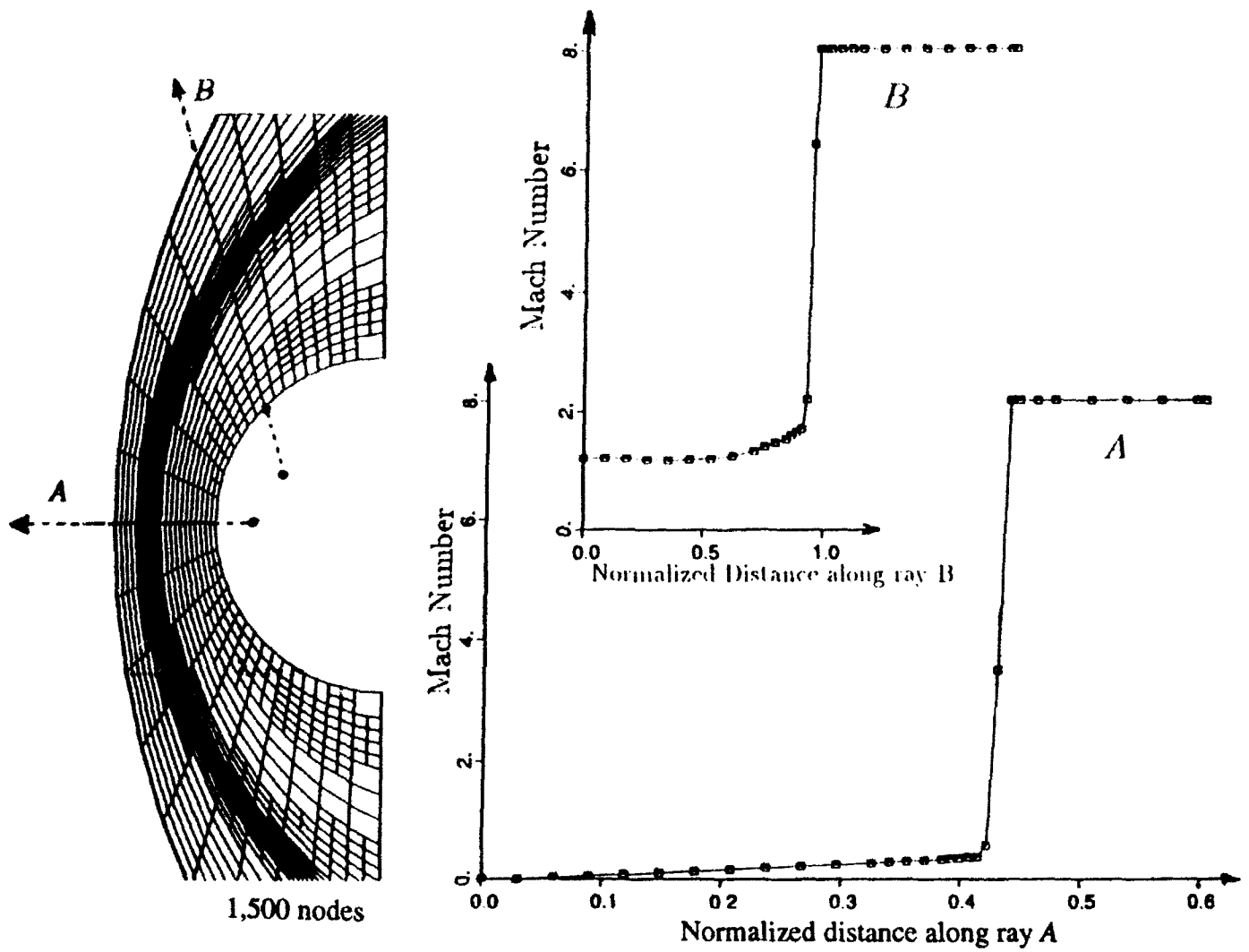


Figure 7. Final adapted mesh (1,500 nodes) and Mach No. distributions along rays *A* and *B* for inviscid 2D flow over circular cylinder.

$$g_{\dot{w}} = \frac{\alpha_L' \alpha_R' + |\alpha_L' \alpha_R'|}{\alpha_L' + \alpha_R' + \delta} \quad (14)$$

which behaves smoothly and is not overly compressive.

This example demonstrates that the method has successfully retained the favorable shock capturing properties associated with the Upwind TVD scheme on structured meshes (see for example Refs. [10, 16, 17 and 4]). Even off centerline - where the shock is not grid aligned - the discrete shock is contained within two cells. Furthermore, the Mach number distributions in each plot cross four grid interfaces, and the conservative treatment described in the preceding section successfully maintains a smooth, nonoscillatory demeanor through these interfaces. Measuring to the sonic point, the shock stand-off distance in this example agrees with the published value to within one grid point [24].

A second inviscid example examines the full 3D formulation and highlights the utility of directional adaptation in three dimensions. Figure 8 provides an overview of a case in which a double wedge corner flow is simulated at $M_\infty=2.98$ with wedge angles $\delta_1=\delta_2=9.49^\circ$. The final mesh contains ~70,000 nodes which is 14 times fewer than the roughly 980,000 which would be required to provide the same shock resolution on a globally refined mesh. Directional division was again permitted at the finest mesh level, and the mesh plane depicted above the grid (at $x=0.8$) shows that the cells have adapted themselves to match the orientation of the wedge and corner shocks. This plane appears again in Figure 9, where contours of constant Mach number are superimposed directly upon both experimental data [25] and a previous inviscid numerical simulation [26]. Additionally, the undisturbed wedge flow away from the corner interaction allows direct comparison with inviscid gasdynamic theory. The agreement with experiment, theory, and prior calculations results is very good, and the shocks span no more than two cells. Figure 10 shows a convergence history for this example showing a net reduction in the global residual of approximately 9 orders of magnitude.

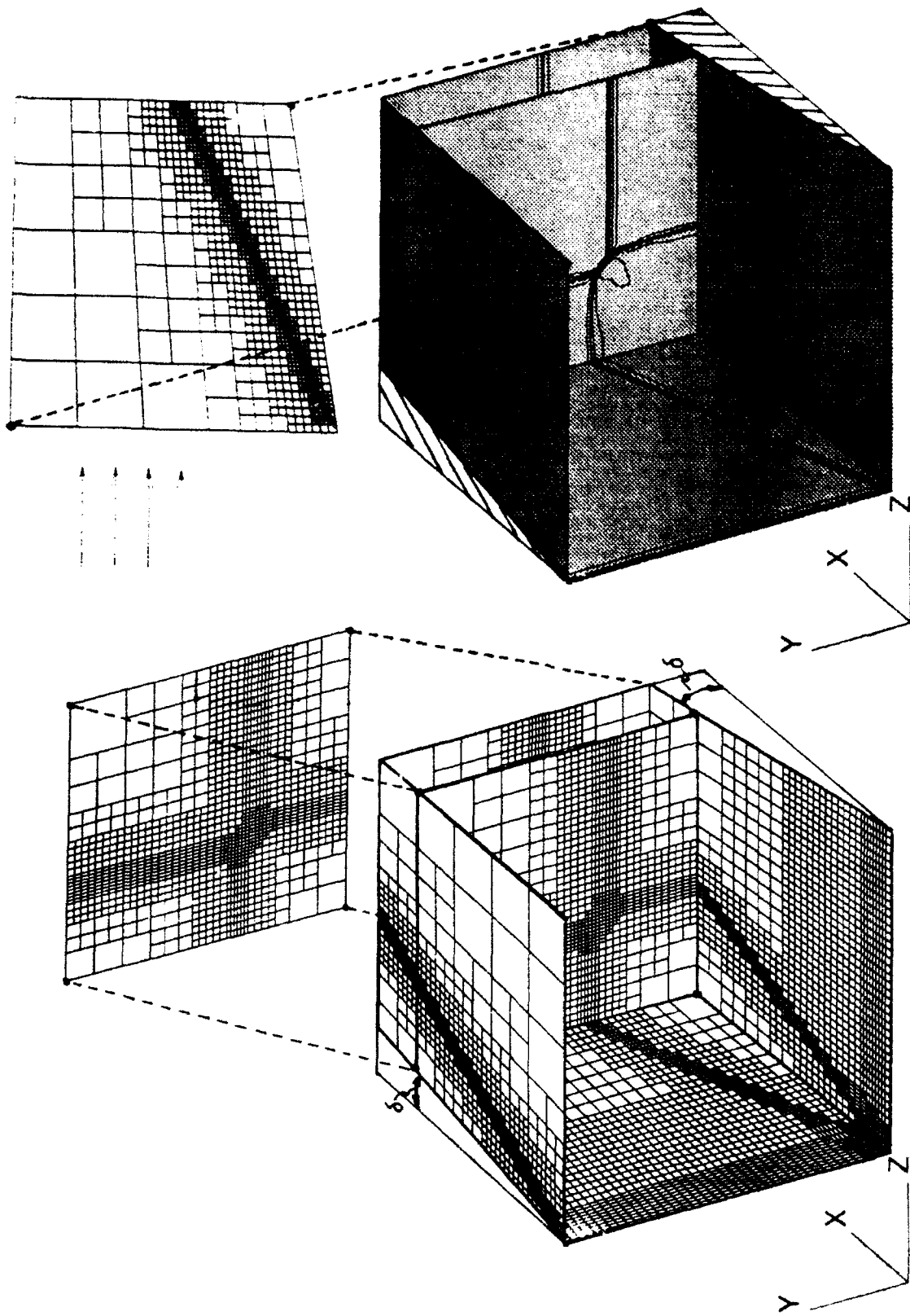


Figure 8. Inviscid double wedge corner flow test case, $M_\infty = 2.98$, $\delta_1 = \delta_2 = 9.49^\circ$, 70,000 nodes.

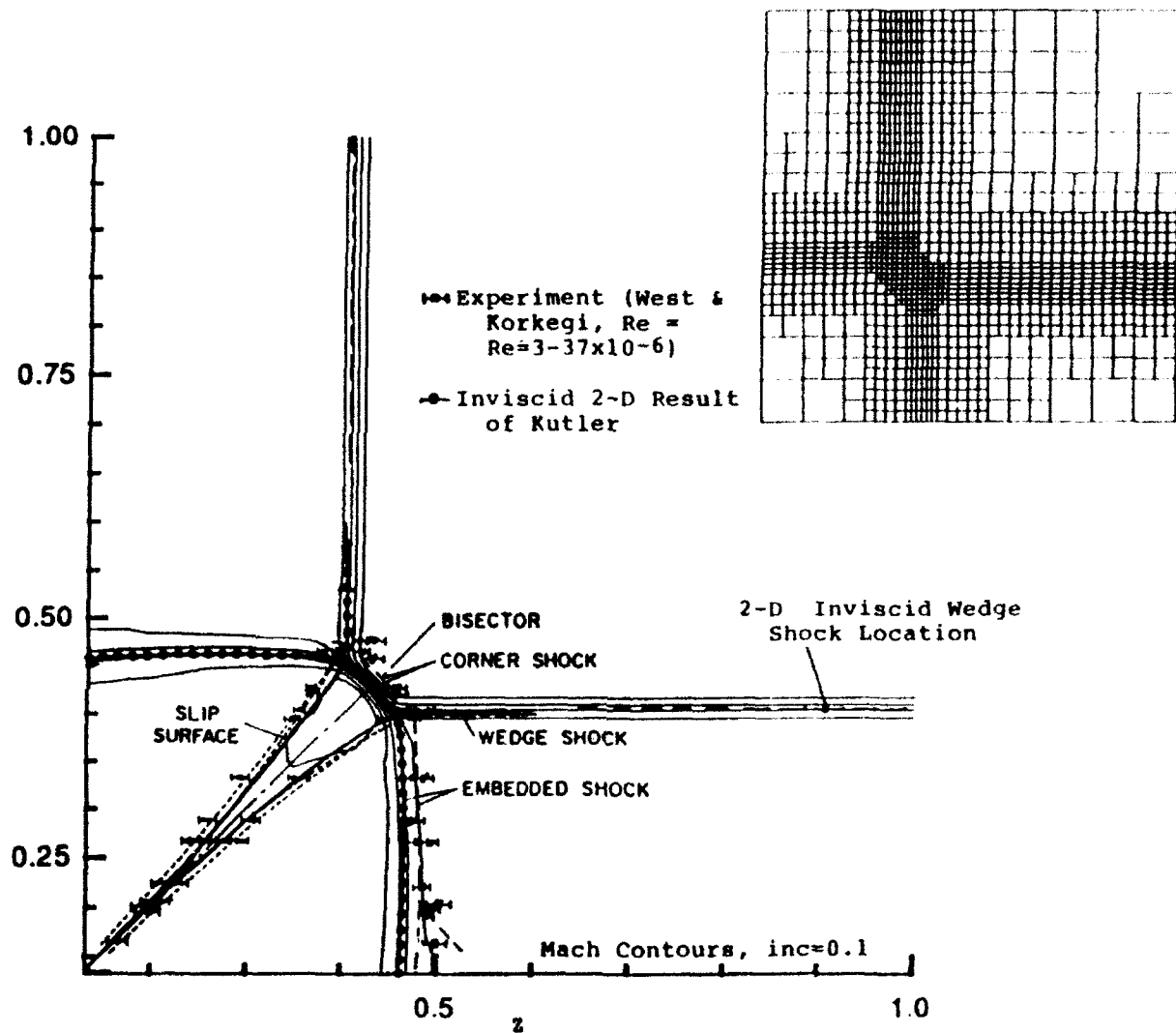


Figure 9. Mach contours in plane at $x = 0.8$ superimposed upon shock positions from inviscid gasdynamic theory [24] experimental data [25] and previous inviscid calculation [26].

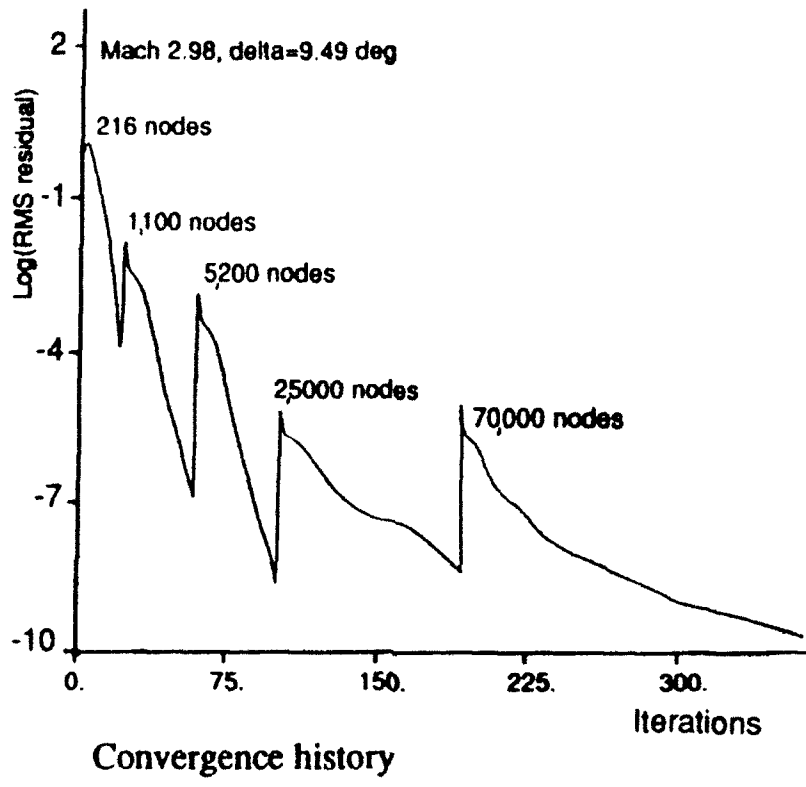


Figure 10. Convergence history of RMS sum of all state vector residuals.

A subsonic flat plate boundary layer provides an initial assessment of the behavior of the viscous discretization. This quasi-2D flow was computed at two levels of resolution using both TVD and central difference operators for $M_\infty=0.5$ and $Re_L=5,000$. This simulation used an entropy cutoff in the TVD scheme of 0.1 and a fourth difference dissipation coefficient of $1/128$ in the central difference calculation. The domain extended $2L$ upstream, along, and above the plate. Figure 11 displays u -velocity profiles of both schemes with 5 and 13 points in the boundary layer. With only five points in the boundary layer, the Upwind TVD method has already essentially reproduced the Blasius profile. This result contrasts sharply with that from the central difference scheme at this level of resolution. With 13 points in the boundary layer, the two integrations produce essentially identical results. At this higher level of resolution, the central difference result produces almost no evidence of the "viscous overshoot" evident in the five point case.

Figure 12 shows skin friction development along the flat plate. This plot reports results for both the central and TVD discretizations at two levels of resolution and compares these with the Blasius relation $C_f=0.664(Re_x)^{-1/2}$. With 13 points in the boundary layer (Re_L of 5,000), the theoretical skin friction is predicted well by about $Re_x = 100$, or 2 percent of the normalized plate length from the leading edge.

4.b Three-Dimensional Viscous Flow

With the basic properties of the algorithm established, Figure 13 opens the presentation of a more complex example aimed at facilitating an evaluation of the feature detection algorithm. Success or failure of the adaptive strategy rests on the ability of this routine to locate and resolve important structures and smooth regions in the flow. Thus, it is important to evaluate the feature detection algorithm on realistically complex, viscous flows at high resolution.

The test case beginning in Figure 13 considers Mach 1.2 flow over the 65° cropped delta wing tested in Ref. [27] at 20° incidence angle. At these conditions, this flow is characterized

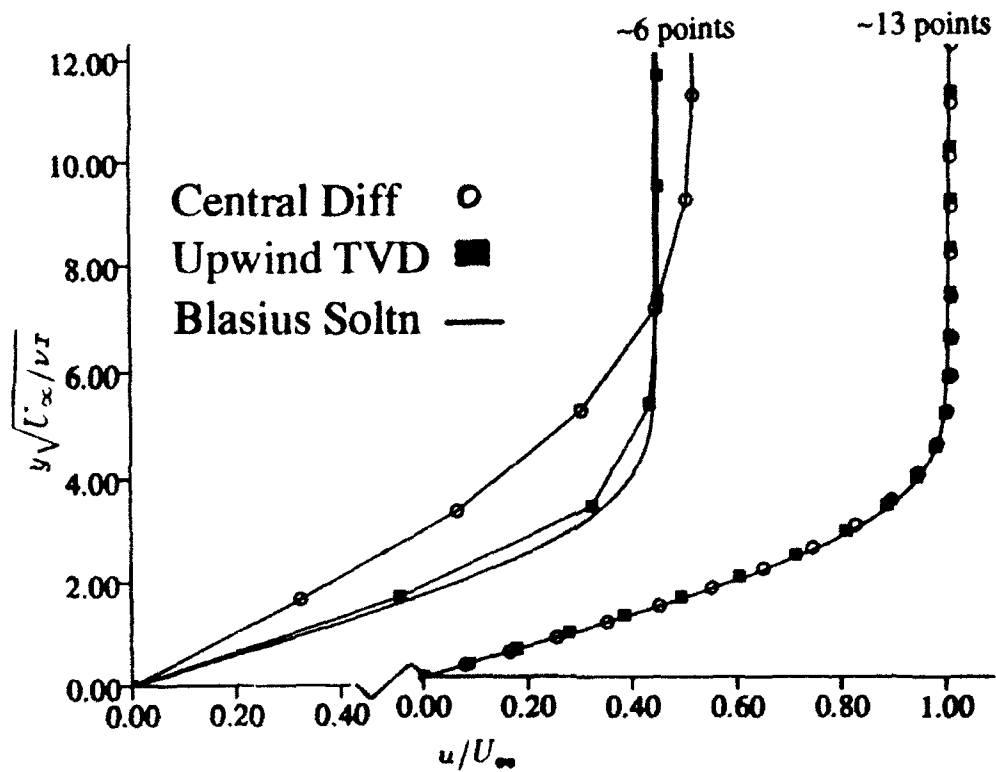


Figure 11. Flat plate boundary layer calculation. $M_\infty = 0.5$, $Re_L = 5,000$. Comparison of u -velocity profile with Blasius solution at various levels of mesh resolution.

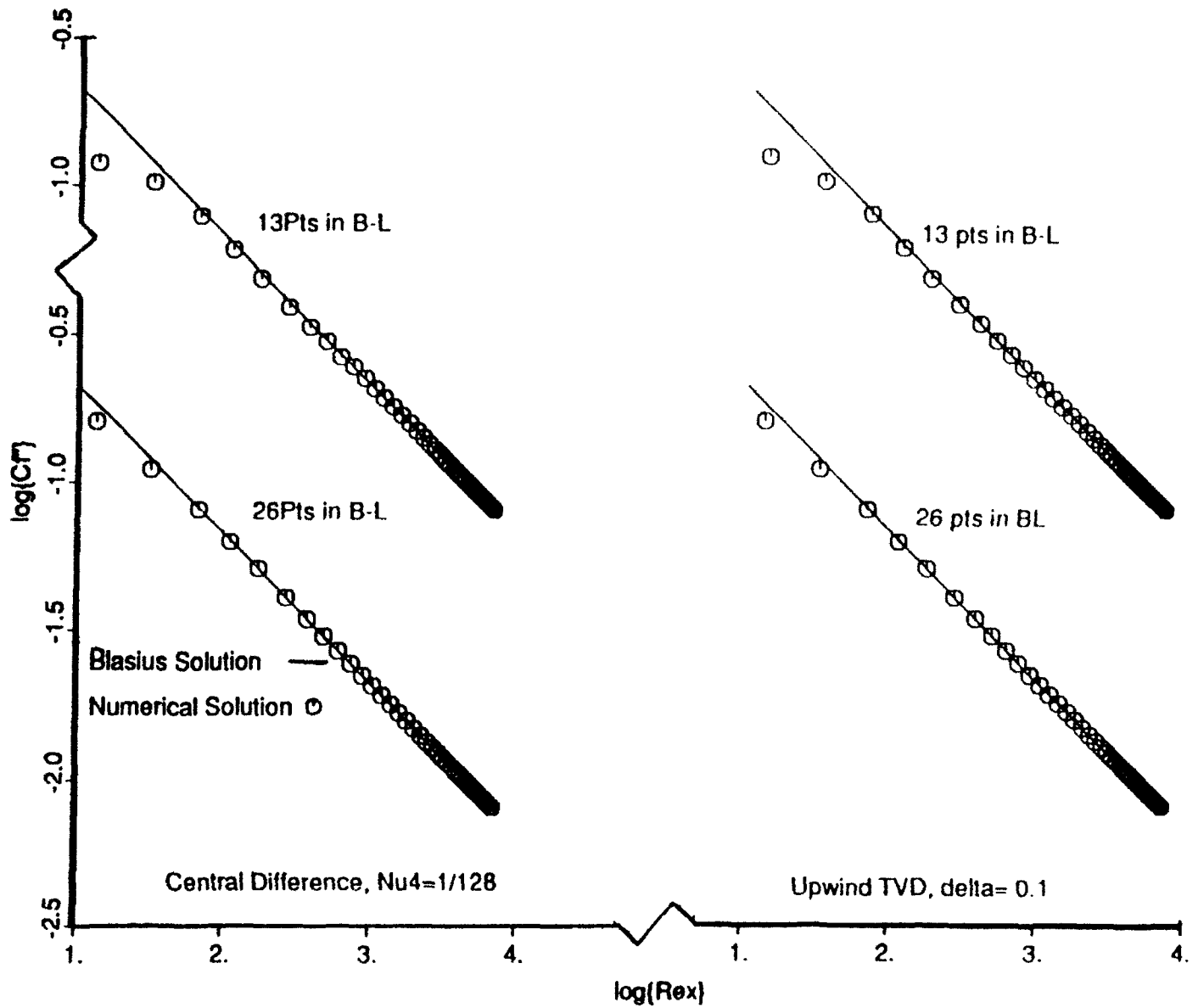


Figure 12. Flat plate boundary layer calculation. $M_\infty = 0.5$, $Re_L = 5,000$. Comparison of skin friction with Blasius solution at various levels of mesh resolution.

by a strong steady primary vortex which separates at the sharp leading edge. Underneath this vortex, a cross-flow shock develops which induces separation of the boundary layer, and "locates" the secondary separation. The tertiary separation lies between the the cross-flow shock and sharp leading edge. On the windward side, a bow shock develops to turn the flow around the wing. This combination of interacting viscous and inviscid features makes this a discriminating problem for evaluating the capabilities of the feature detection algorithm for realistic, complex 3D flows.

The laminar, half-span calculation used a Reynolds number of 480000 based on the root chord, while the experiment was conducted at $Re_C=2.4-5.3 \times 10^6$. The wing in the calculation was not truncated at the trailing edge, but instead, was extended downstream to the outflow boundary (located at approx. $x=1.1c$).

Figure 13 contains an overall view of the computation. The wing is depicted with the mesh on the starboard and density contours on the port side of the delta wing. These contours show the footprints of the primary vortex, cross-flow shock, secondary and tertiary vortices on the wing surface. The final adapted mesh used 999,000 nodes, placing about 260 points chordwise and 150 points spanwise (at the trailing edge) on the upper surface of the wing. Figure 14 shows further details of the flow as it passes through the plane located at the trailing edge through contours of total pressure loss. The figure clearly shows the adaptation pattern responding to capture the shock triggered separation underneath the primary vortex, as well as resolution of feeding sheet and the entrained tip vortex. This indicates that the feature detector successfully located these weaker features, while still responding to the strong vortical structures and bow shock. Figure 15 contains symmetry plane Mach contours, and a view of the corresponding adapted grid while Figure 16 compares this calculation with wind tunnel results from Ref. [27]. The computed surface streamlines reproduce the overall surface shear pattern from the experimental oil flow visualization including formation of the secondary and tertiary separations. The tertiary vortex in the calculation does not appear to

Density Contours, inc=0.025

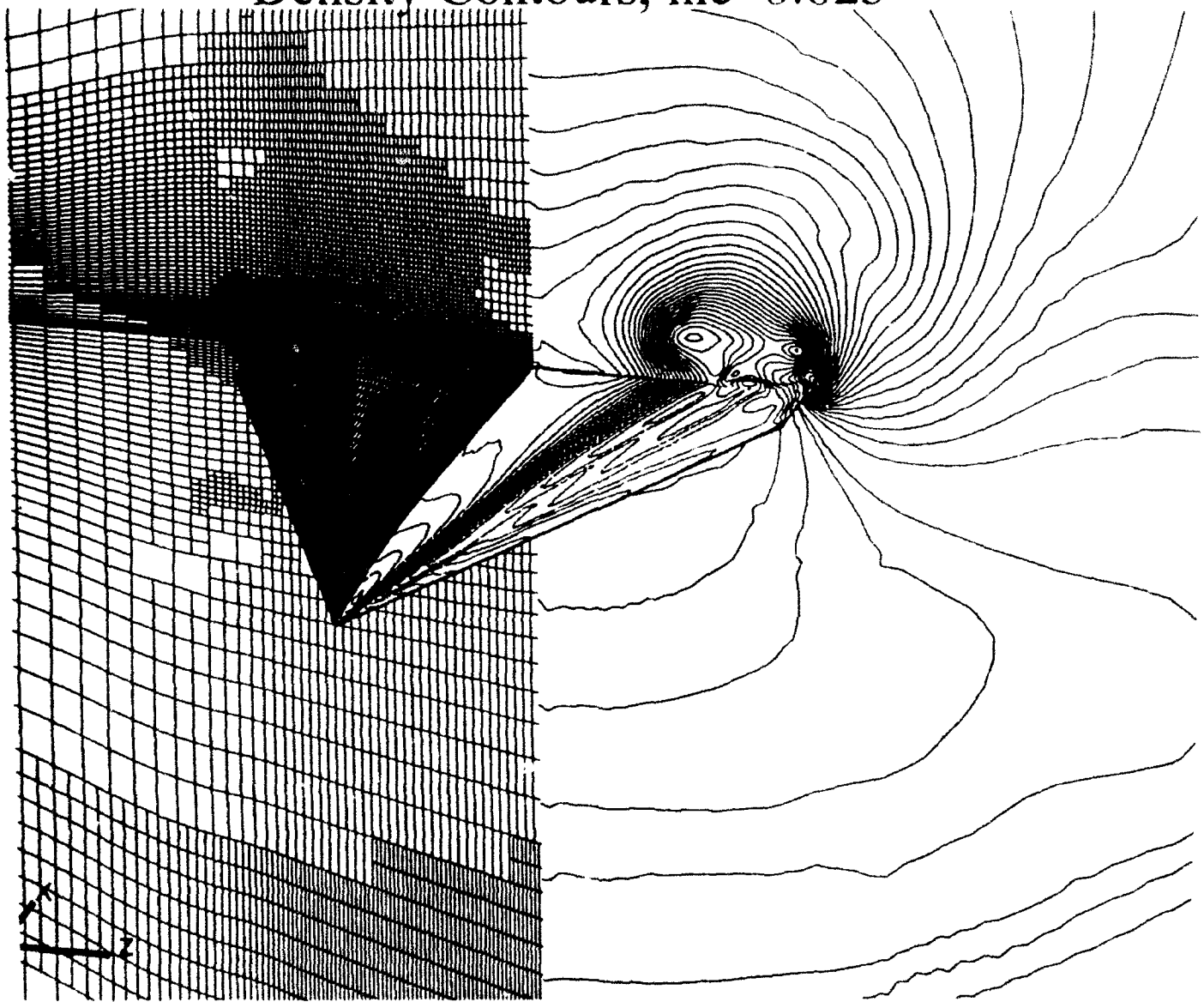


Figure 13. Navier-Stokes solution of supersonic flow over delta wing of Ref [27] at $M_\infty = 1.2$, $Re_C = 480,000$, $\alpha = 20^\circ$ with 999,000 nodes.

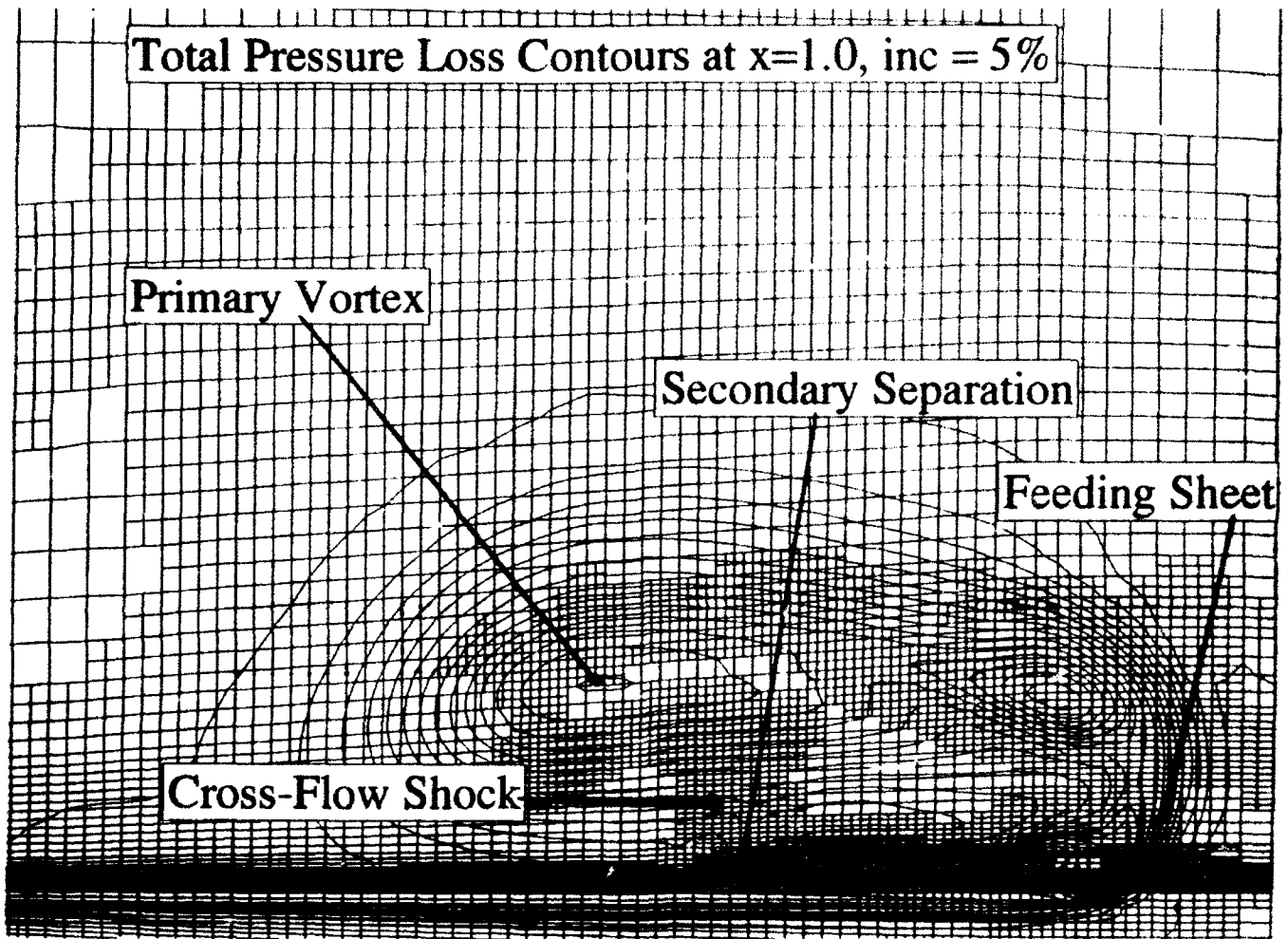


Figure 14. Total pressure loss contours at t.e. ($x = 1.0$) showing shock induced separation.

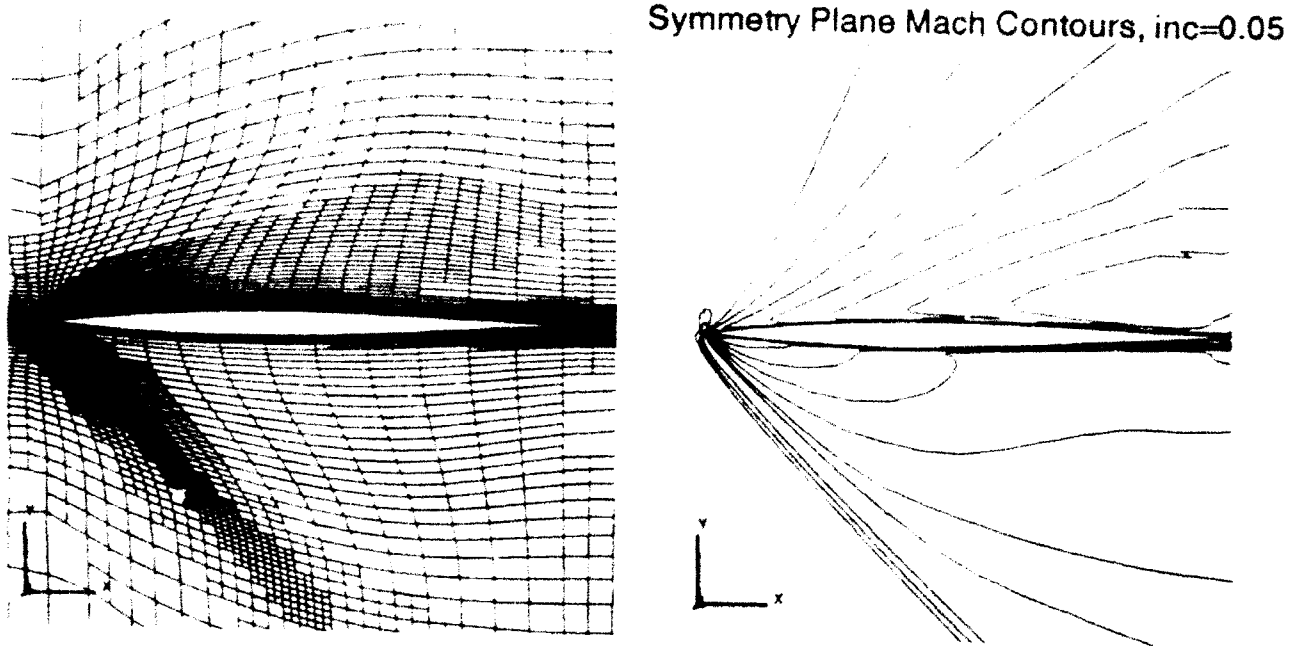


Figure 15. Mesh and Mach contours in symmetry plane.

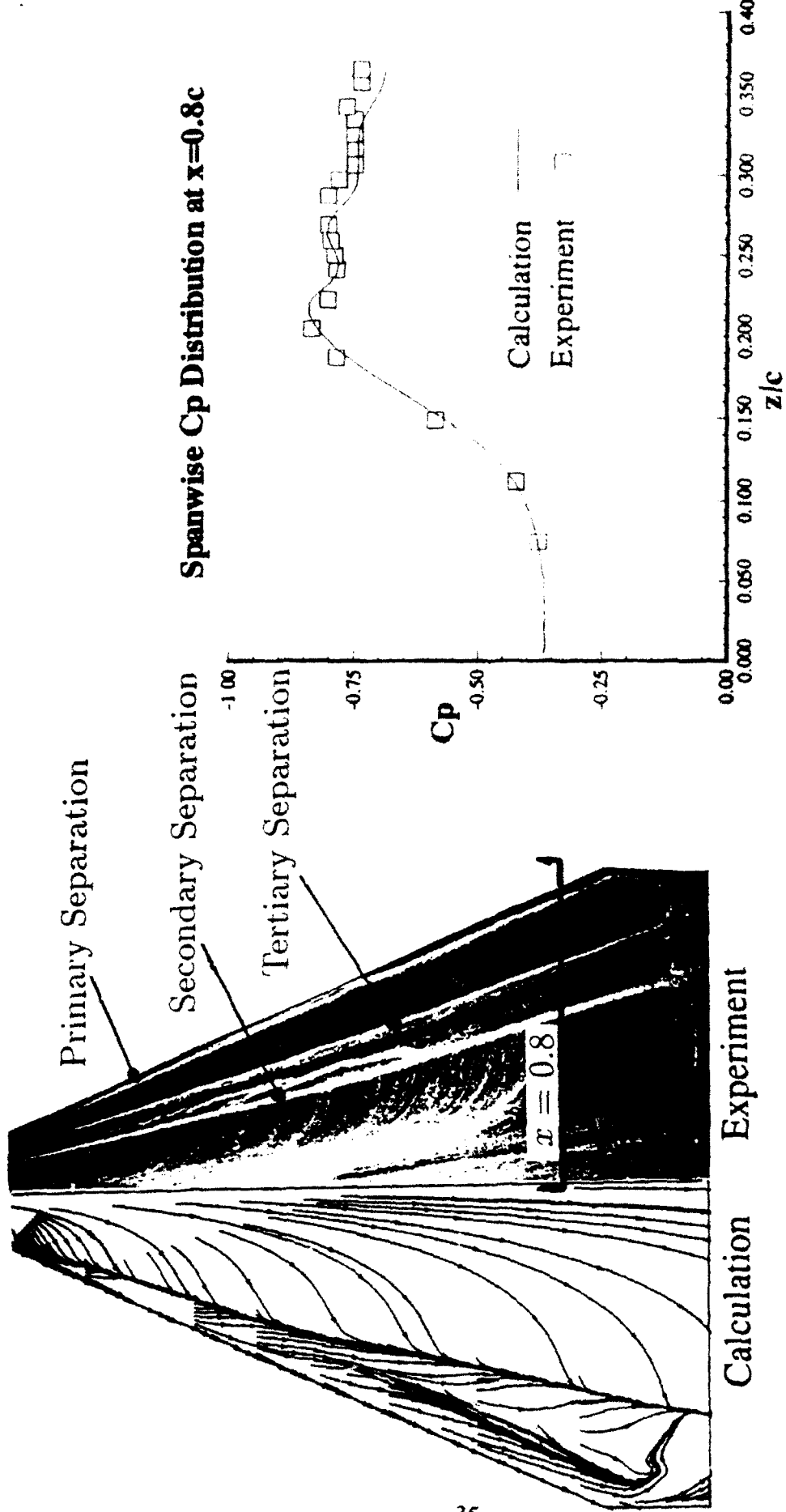


Figure 16. Right: Results from experimental oil flow visualization [27] ($Re_C = 2.4-5.3 \times 10^6$). Left: Computed surface streamlines from numerical solution ($Re_C = 4.8 \times 10^5$). Left: Comparison of C_p at $x = 0.8$ with experimental results from Ref. [27].

form quite as early or as fully as in the experiment, and this is believed to be a Reynolds number effect. Figure 16 also contains a direct comparison of the C_p distribution at $x=0.8c$ with experimental measurements. Starting at the symmetry plane, the line plot agrees with the data underneath the primary, through cross-flow shock and secondary separation point, and begins to differ only in the location of the tertiary separation. Despite the Reynolds number difference, this comparison is quite reasonable. Nevertheless, it should be re-emphasized that this example was completed to focus on the performance of the detection algorithm and was not conducted as a rigorous attempt to reproduce wind tunnel data.

4.c Processing Efficiency and Storage

The 3D Navier-Stokes solver has been ported to Cray X-MP, Y-MP, and Cray 2 platforms. The main iteration loop is completely vectorized, including the numerical flux calculation and the computation of viscous fluxes. No explicit edge or cell coloring schemes were employed to achieve this result. Instead, a coloring is implied by sequential sweeps over corresponding faces of all cells (i.e., all N faces, all S faces, etc.). Some of the loops within the viscous flux calculation required "unwinding" by hand to vectorize these routines, but no other special coding was required.

After loading a restart file and preprocessing all geometric calculations (surface vectors, cell volumes, etc.), timing tests were run on 500 iterations of the 999,000 node 65° cropped delta wing presented in the preceding set of figures. This example contained 50,000 boundary nodes and the boundary conditions were not fully vectorized. With the TVD option chosen, the Navier-Stokes simulation proceeded at $70\mu\text{sec}/\text{node}/\text{iteration}$ on single processor of the X-MP. Selecting central differencing for the inviscid fluxes results in Navier-Stokes simulations at $30\mu\text{sec}/\text{node}/\text{iteration}$. Careful timings were not completed on either the Cray 2 or the Y-MP.

The solver currently stores 153 words/node for full upwind Navier-Stokes simulations. 30 words/node of this storage are required for the precalculation of the difference of characteristic variables across all cell faces (as discussed in Section 2), and thus, the central difference scheme requires approximately 125 words/node. On a per-node basis, the scheme requires 3-4 times more storage than an efficiently written structured solver. Adaptive methods hope to offset this by using fewer nodes to obtain discrete solutions of comparable accuracy. The 3D examples presented earlier in this section require roughly an order of magnitude fewer grid points than an equivalently resolved structured mesh solution. Additionally, the use of fewer nodes not only reduces storage requirements, but also decreases the time required per time step, since fewer nodes must be integrated. With the exception of local time stepping, no acceleration techniques were applied to the basic solver. A host of such techniques exist for accelerating Runge-Kutta schemes, and the next section discusses likely candidates for incorporation.

5. Summary and Future Work

A second-order upwind method for solution of the 3D Navier-Stokes equations was formulated on adaptively embedded meshes. This implementation permits local adaptation through cell division in response to emerging flow features. The feature detection algorithm separates the detection of shocks from that of other flow phenomena and can divide cells directionally in response to local resolution requirements.

Application of the method to several inviscid and viscous test problems pointed out the ability of the method to provide accurate solution to examples with high resolution requirements. These examples demonstrated that the unstructured method retains the crisp, nonoscillatory shock representation associated with TVD schemes on structured meshes. Simulation of laminar, viscous flows highlighted the ability of the full Navier-Stokes solver to accurately model viscous flow by comparison with both theoretical and experimental results in both two and three dimensions.

With the preliminary developmental work on this solver complete, further efforts will focus on improving the flexibility and utility of the method. The Runge-Kutta time stepping and embedded mesh topology make multigrid acceleration a natural choice for increasing the convergence efficiency of the method. Additionally, such work should examine possibilities for domain decomposition and implicit temporal integration. Finally, future investigations will also explore the practicality of applying the method to complex configurations using block-structured initial meshes.

6. References

- [1] Yee, H. C. "Upwind and Symmetric Shock-Capturing Schemes," *NASA - TM 86842*, 1987.
- [2] Harten, A., "High Resolution Schemes for Hyperbolic Conservation Laws," *Journal of Computational Physics*, Vol. 43, pp. 357-393, 1983.
- [3] Roe, P. L., "Approximate Riemann Solvers, Parameter Vectors, and Difference Schemes," *Jol. of Computational Physics*, Vol. 43, 1981.
- [4] Kroll, N., Gaitonde, D., and Aftosmis, M., "A Systematic Comparative Study of Several High Resolution Schemes for Complex Problems in High Speed Flows," *AIAA Paper - 91-0636*, 1991.
- [5] Ramanurti, R., and Löhner, R., "Simulation of Subsonic Viscous Flows using Unstructured Grids and a Finite Element Solver," *AIAA-90-0702*, 1990.
- [6] Aftosmis, M., and Kroll, N., "A Quadrilateral Based Second-Order TVD Method for Unstructured Adaptive Meshes," *AIAA 91-0124*, 1991.
- [7] Dannenhoffer, J. F., III, and Baron, J. R., "Adaptation Procedures for Steady-State Solution of Hyperbolic Equations," *AIAA -84-0005*, 1984.
- [8] Kallinderis, Y., and Baron, J. R., "Adaptation Methods for a New Navier-Stokes Algorithm," *AIAA 87-1167*, 1987.

- [9] Mavriplis, D. J., "Multigrid Solution of the Navier-Stokes Equations on Triangular Meshes," *AIAA Jol.* Vol.28, No. 8, 1990.
- [10] Yee, H. C., Harten, A., "Implicit TVD Schemes for Hyperbolic Conservation Laws in Curvilinear Coordinates," *AIAA Jol.*, Vol 25, 1987.
- [11] Roe, P. L., and Beard, L., "An Improved Wave Model for Multidimensional Upwinding of the Euler Equations," *Proceedings of the 13th International Conference on Numerical Methods in Fluid Dynamics*, Rome, Italy, 1992.
- [12] Rumsey, C., van Leer, B., and Roe, P. L., "A Grid-Independent Approximate Reimann Solver with Applications to the Euler and Navier-Stokes Equations," *AIAA-91-0239*, 1991.
- [13] Barth, T. J., Jespersen, D.C., "The Design and Application of Upwind Schemes on Unstructured Meshes," *AIAA - 89-0366*, 1989.
- [14] Durlofsky, L. J., Osher, S. and Enquist, B., "Triangle Based TVD Schemes for Hyperbolic Conservation Laws," *ICAS Report 90-10*, 1990.
- [15] Jameson, A., "A Vertex Based Multigrid Algorithm for Three-Dimensional Compressible Flow Calculations," in *Numerical Methods for Compressible Flows - Finite Difference, Element, and Volume Techniques*, Ed. by T.E. Tezduar and T. Hughes, Applied Mechanics Div. 78, ASME, NY, 1986.
- [17] Kroll, N., and Rossow, C., "A High Resolution Cell Vertex TVD Scheme for the Solution of the Two- and Three-Dimensional Euler Equations," *Proceedings of the 12th Conference on Numerical Methods in Fluid Dynamics*, Oxford, UK, 1990.
- [18] Barth, T. J., "Aspects of Unstructured Grids and Finite-Volume Solvers for the Euler and Navier-Stokes Equations," *AGARD Report 787*, May 1992.

- [19] Aftosmis, M., "Viscous Flow Simulation Using an Upwind Method for Hexahedral Based Adaptive Meshes," *AIAA-93-0772*, 1993.
- [20] Kallinderis, Y. G., "Adaptation Methods for Viscous Flows," PhD. Thesis Massachusetts Institute of Technology, Dept. of Aeronautics and Astronautics, Cambridge, MA, 1988.
- [21] Radespiel, R., Rossow, C., and Swanson, R. C., "Efficient Cell-Vertex Multigrid Scheme for the Three-Dimensional Navier-Stokes Equations," *AIAA Jol.*, Vol. 28, No. 8, pp. 1464-1472, 1990.
- [22] Martinelli, L., "Calculations of Viscous Flows with a Multigrid Method," *Ph.D. Thesis*, Dept. of Mechanical and Aerospace Engineering, Princeton Univ., 1987.
- [23] Warren, G. P., Anderson, W., K., and Krist, S., "Grid Convergence for Adaptive Methods," *AIAA-91-1592-CP*, 1991.
- [24] Hays, W. D., and Probstein, R. F., *Hypersonic Flow Theory; Volume I: Inviscid Flows*. Academic Press, 1966.
- [25] West, J. E., and Korkegi, R. H., "Supersonic Interactions in the Corner of Intersecting Wedges at High Reynolds Numbers," *AIAA Jol.* Vol. 10, No. 5, May 1972.
- [26] Kutler, P., "Supersonic Flow in the Corner by Two Intersecting Wedges," *AIAA Jol.* Vol.12, pp. 577-578, 1974.
- [27] Erickson, G. E., Schreiner, J. A., Rogers, L.W., "On the Structure, Interaction, and Breakdown Characteristics of Slender Wing Vortices at Subsonic, Transonic, and Supersonic Speeds," *AIAA-89-3345*, 1989.

Nomenclature

δ	small parameter preventing zero wave speed, $\delta \ll 1$
e	total internal energy per unit mass
λ	eigenvalue of flux Jacobian matrix
u, v, w	Cartesian velocity components
p	local static pressure
Rs	shock refinement parameter
ρ	density
T	threshold for cell division
V_i	volume of cell i
\bar{F}	complete flux density tensor
\bar{g}	limiter function
\bar{n}	unit normal vector $[n_x, n_y, n_z]^T$
\bar{S}_k	surface vector of face k . $[S_x, S_y, S_z]^T_k$
\bar{Q}_k	vector of numerical flux through face k
\bar{U}	state vector $[\rho, \rho u, \rho v, \rho w, e]^T$
$\bar{\Phi}_k$	limited flux function at face k
\mathfrak{R}	right eigenvector matrix of flux Jacobian in transformed space